RESEARCH ARTICLE

NANO · MICRO small
www.small-journal.com

Moiré-Induced Enhanced Hydrogen Adsorption on Graphene

*Daniel Arribas, Adrián Sáez-Coronado, Borja Cirera, Natalia Blanco, José Ignacio Martínez, Alejandro Gutiérrez, José Ángel Martín-Gago, Irene Palacio, and Pablo Merino**

The periodic patterning induced by moiré superstructures enables the synthesis of spatially functionalized graphene surfaces owing to changes in the local reactivity of the material. However, quantitative characterization of the effect of different moiré patterns remains elusive. By exploiting the large number of moiré superstructures appearing on epitaxial graphene grown on a Pt(111) surface, this stud examines the effect of moiré-induced corrugation on the local reactivity toward hydrogenation. This work combines atomically resolved scanning tunneling microscopy alongside density functional theory and Monte Carlo simulations of hydrogen chemisorption. The findings reveal a more efficient hydrogen adsorption onto moiré patterns compared to flat graphene, with a marked selectivity toward the most topographically protruding areas of the moiré. This moiré-induced enhancement of the hydrogenation efficiency is slightly increased on the most corrugated structures, which also display longer residence times and a higher stability against thermal desorption.

1. Introduction

Graphene is an exceptional material in terms of mechanical and electronic properties. This 2D material benefits from an extremely high chemical stability, derived from its polyaromatic character.[1] While the absence of a bandgap in its electronic structure has a beneficial impact for those applications in which high carrier mobilities are required (such as in the fabrication of transparent electrodes or devices operating at high frequencies), it limits the suitability of this material for other applications, such as electronic digital devices. To overcome these limitations and tune the properties of this material, the chemical functionalization of graphene stands as a key strategy. This approach has prompted the application of graphene in a wide range of fields, including optoelectronics, medical and sensing devices,[2] or energy storage.[1,3] Nonetheless, the low chemical reactivity of graphene hinders its chemical modification for these purposes.

Up to date, several strategies have been explored to control the reactivity of graphene, for example, by inducing strain to the material,[4,5] functionalizing it with catalytic materials,[6,7] or creating defects in the graphene lattice.[8,9] Moiré patterns have been observed to play a role in the reactivity of 2D materials in general (for example, in the case of WS_2 MoS_2 for the hydrogen evolution reaction)[10,11] and graphene in particular.[12–16] These periodic patterns arise from the mismatch between two superimposed lattices, such as in the case of two rotated graphene sheets, or when this material is grown on a metallic substrate. The unique moiré periodicities enable the synthesis of spatially functionalized graphene surfaces owing to changes in the local reactivity of the material.[1] For example, the periodic adsorption of H atoms on the moiré-patterned graphene on Ir(111) leads to the apparition of an electronic gap around the Fermi level,[17] whereas hydrogenation and H intercalation in epitaxial graphene on Ru(0001) produce a functionalization following a honeycomb pattern.[18]

In this work, we investigate how different moiré patterns affect the hydrogenation of graphene by means of the deposition of thermally cracked H atoms under ultra-high vacuum conditions. The adsorption of H atoms in this way can be considered a probe of the local reactivity of graphene on its own.[19] Previous fundamental works, both experimental and theoretical, of graphene hydrogenation on several substrates such as Ir(111), SiC(0001) or HOPG have provided useful information, such as the preference of H atoms for adsorption in clusters, typically dimers (two atoms bonded to the same carbon hexagon), or the local shift from sp^2 hybridization to a tetrahedral sp^3 configuration occurring upon H chemisorption. When a hydrogen atom bonds to a carbon atom

D. Arribas, A. Sáez-Coronado, B. Cirera, N. Blanco, J. I. Martínez, J. Á. Martín-Gago, I. Palacio, P. Merino
Instituto de Ciencia de Materiales de Madrid (ICMM-CSIC)
c/ Sor Juana Inés de la Cruz, 3, Madrid 28049, Spain
E-mail: pablo.merino@csic.es

A. Gutiérrez
Universidad Autónoma de Madrid
c/ Francisco Tomás y Valiente, 7, Madrid 28049, Spain

The ORCID identification number(s) for the author(s) of this article can be found under https://doi.org/10.1002/smll.202507323

DOI: 10.1002/smll.202507323

on the surface, it induces a local change from the original planar sp^2 configuration to a tetrahedral sp^3 configuration with the hydrogen atom positioned on top of the carbon atom.[20,21] This change requires puckering the carbon atom out of the graphene plane, which is energetically unfavorable. Interestingly, the local curvature of the graphene can reduce this energy penalty if the graphene sheet is bent so that the C atom is already protruding toward the H atom, essentially changing the local reactivity toward hydrogenation. In this way, the binding energy of H atoms in the convex areas of a deformed graphene increases, as it has been experimentally proven for nanotubes or fullerenes[21–24], and for individual graphene moiré patterns.[13,20,25]In addition, in the case of epitaxial graphene, interaction between C atoms and the substrate in areas where the registry is adequate can further stabilize the hydrogenated configurations. All in all, the reactivity of graphene is dependent on a plethora of structural factors.

Corrugated moiré superstructures, arising from the mismatch between the stacked lattices of the graphene and the substrate, offer an excellent platform for a fundamental study of the effects of periodically nanostructured graphene on hydrogen adsorption. In previous experimental surface science works, the focus has been typically placed on single moiré patterns, such as the $(9 \times 9)R0°$ on the Ir(111),[13] (11×11) R0° on Ru(0001),[18] or the $(6\sqrt{3} \times 6\sqrt{3})R30°$ on SiC.[26] Over these substrates, typically only one moiré is obtained, which limits the comparative study between patterns with different periodicities on the same substrate. However, different moiré periodicities can result in different properties, such as different corrugations or the opening of different band gaps. Unfortunately, on epitaxial graphene sheets, it is generally impossible to control the moiré patterns obtained, which are dictated by the interaction between graphene and substrate.

Depending on its orientation with respect to the substrate, graphene grown on a Pt(111) surface exhibits 22 different stable moiré superstructures, each one of them defined by the angle between the substrate and graphene lattices, which can coexist in the same sample, forming domains (see Section S1, Supporting Information).[27] This remarkable variety allows us to explore the influence of a wide range of structural parameters of the moiré physics, and moiré corrugation in particular, on hydrogen adsorption. Although graphene weakly interacts with the platinum surface (it adsorbs at a height > 3 Å, and its electronic structure resembles that of free-standing graphene, apart from a slight *p*-doping),[28] this interaction is enough to induce structural corrugations on the graphene in the range from 0 to 0.40 Å, depending on each particular moiré superstructure.[29] In general, there are two types of moiré patterns in the system graphene/Pt(111): non-corrugated (corrugation close to 0 Å), which present small lattice parameters below 11.3 Å, and highly corrugated (corrugation between 0.10 and 0.40 Å), which present larger lattice parameters.[30] The competition between the increased binding energy of moiré superstructures and the energy necessary to deform the graphene determines the final corrugation of the graphene sheet.[30] The coexistence of stable moiré domains with clearly different corrugations, together with the weak interaction between graphene and substrate, makes this system an ideal model for the fundamental study of H adsorption on nano-patterned graphene sheets.

In this work, we employ a combined approach of experimental characterization by Scanning Tunneling Microscopy (STM) at both room temperature (RT) and 10 K along with *ab initio* calculations to provide a fundamental understanding of the chemisorption of atomic H on epitaxial graphene monolayers grown by decomposition of fullerenes on a hot Pt(111) surface. By confronting our experimental data with a variable-step kinetic Monte Carlo model, considering the curvature of each moiré superstructure, we evaluate the adsorption efficiency, hydrogen residence time, and desorption kinetics at a working temperature of 400 K. Our results demonstrate that corrugated moirés present both enhanced adsorption efficiency and a better stability at higher temperatures compared to a flat graphene sheet. Additionally, the degree of moiré-induced enhancement in hydrogen adsorption efficiency is significantly pronounced on the most corrugated patterns with larger lattice parameters.

2. Results and Discussion

We conduct an extensive characterization of hydrogen chemisorption on ten different moiré domains after exposing the samples at room temperature to a dose equivalent to 0.12 monolayers of dissociated H_2 molecules under ultra-high vacuum (UHV) conditions (**Figure 1**a–j). The molecular dissociation was activated by thermal cracking in a commercial system consisting of a tungsten capillary heated at 2300 K by electron bombardment. At these coverages, the graphene moiré superstructures remain unaffected and clearly identifiable in STM images. Hydrogen appears as multi-lobed protrusions with lateral sizes ranging from 0.5 to 1.5 nm of length (see Figure 1k–n). We assign these features to clusters of chemisorbed hydrogen atoms, in agreement with previous works.[26,31–33] The apparent lateral size of these clusters is much larger than what can be expected from single hydrogen atoms, since the charge transferred from the H atoms to the C atoms pins into states surrounding the Dirac point that involve several neighboring carbon atoms (see Figure 2h).[34] Once the clusters are formed, they remain stable over days at room temperature and UHV conditions. However, we observe that strong electric fields or interaction with the STM tip during measurements can induce local desorption from the surface (Figure S2, Supporting Information).[32,35] Interestingly, we notice that the H clusters consistently appear at the brightest parts of the moiré superstructure, as it can be appreciated in those with a larger lattice parameter (Figure 1e–j). In epitaxial graphene grown on Pt(111), these parts correspond to those areas of the graphene with a convex curvature, which are topographically more protruding according to previous experimental and theoretical results.[29]

Even though the exact configuration of the clusters is difficult to establish solely from STM images, we tentatively assign them to *ortho*- or *para*-dimers, since they are more stable than the monomers or the *meta* dimers (2.7–2.9 eV for *ortho*- and *para*-dimers to be compared with 0.8–1.6 eV for *meta*-dimers, see Section S6.4, Supporting Information).[25,36–40] Occasionally, we observe how a whole cluster desorbs from the surface while scanning (see Section S3, Supporting Information). On the other hand, we do not observe any cluster diffusion independently of the moiré pattern onto which they are bonded, as expected from the high energy barriers for hydrogen diffusion on graphene in

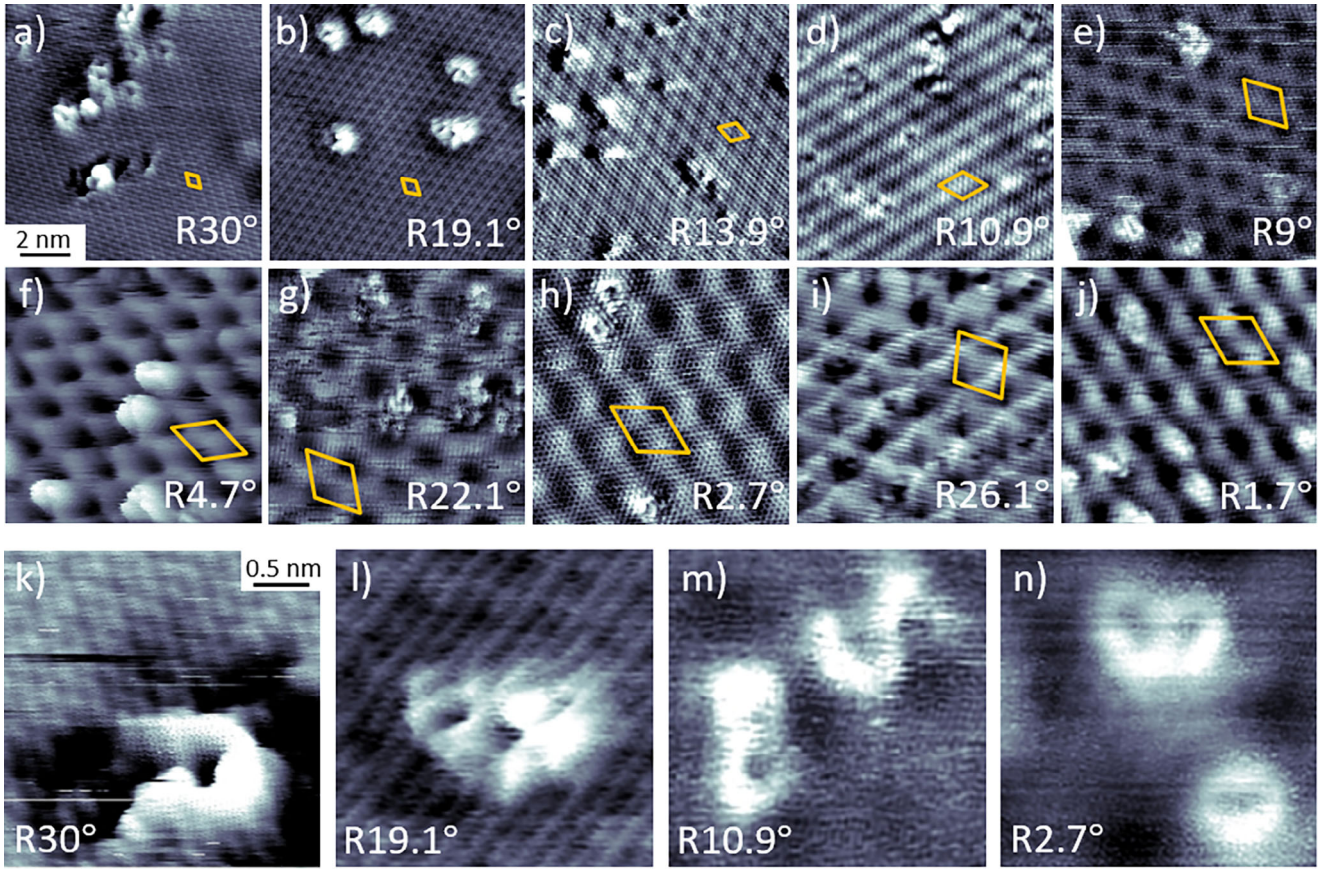

Figure 1. STM images of different moiré superstructures, in increasing lattice parameter order, after deposition of 0.12 Langmuirs of atomic hydrogen/deuterium. Each moiré is denoted by the angle of rotation of the graphene with respect to the substrate. All images were acquired at room temperature except for panels c), d), which were acquired at 10 K. The corresponding supercells are highlighted with an orange rhombus in each panel. Hydrogen atoms form clusters that appear as bright features with multiple lobes and dark spots. All images in the first two rows are 10 nm × 10 nm and correspond to the following moirés: a) R30°, $I = 2.72$ nA, $V = -250$ mV, b) R19.1°, $I = 1.35$ nA, $V = -250$ mV, c) R13.9°, $I = 0.95$ nA, $V = -240$ mV ($T = 10$ K), d) R10.9°, $I = 0.90$ nA, $V = 250$ mV ($T = 10$ K), e) R9°, $I = 1.27$ nA, $V = -450$ mV, f) R4.7°, $I = 0.29$ nA, $V = 18$ mV, g) R22.1°, $I = 1.00$ nA, $V = -1150$ mV, h) R2.7°, $I = 1.86$ nA, $V = -490$ mV, i) R26.1°, $I = 4.15$ nA, $V = 310$ mV, and j) R1.7°, $I = 1.50$ nA, $V = -950$ mV. In Table S1 (Supporting Information), we include more details on our moiré notation.[27] Panels k), l), m), n) are high-resolution images (2.5 nm × 2.5 nm) from clusters on moiré R30° ($I = 1.40$ nA, $V = -240$ mV), R19.1° ($I = 1.35$ nA, $V = -250$ mV), R10.9°, and R2.7° ($I = 0.16$ nA, $V = -450$ mV) respectively. See also Figure S2 (Supporting Information).

the order of 1 eV.[41,42] The clusters present some identifiable inner structure (see Figure 1k–n; Figure S2, Supporting Information). In high-resolution images, sets of dark spots are apparent inside the clusters, attributable to the hydrogen atoms themselves, in agreement with simulated STM images obtained from our Density Functional Theory (DFT) calculations (see Section S4, Supporting Information for more details).

The apparent topography of the moiré superstructures and the dimers exhibits a dependence on the bias voltage, as shown in **Figure** 2a–d for the moiré R4.7°. The apparent topographic height of the graphene moiré increases from approximately 2 Å (from peak-to-peak) at −32 mV to roughly 4 Å at 10 mV. At the same time, the apparent height of the H dimers remains without a clear bias voltage dependence. Overall, the increase of the apparent corrugation of the moiré pattern overshadows the H clusters, rendering them dimmer in comparison. We reproduce this observation in an STM-image simulation for a single H atom chemisorbed on the R30° superstructure (see Section S5, Supporting Information).[27] In Figure 2e, we show Scanning Tunneling Spectroscopy (STS) experiments conducted at 10 K on a moiré R10.9° domain after deposition of atomic hydrogen (see Table S1, Supporting Information for more details on this nomenclature). On the pristine graphene, the conductance, dI/dV, shows a rounded valley shape with its minimum at +325 mV (to be compared with the DFT-predicted +310 mV for the R30° superstructure). We assign this to the Dirac point, indicating a slight *p*-doping, which is in agreement with angle-resolved photoemission spectroscopy measurements.[43] This spectrum is the result of probing both the states from the graphene and the Pt(111) substrate. By performing STS on a H cluster we obtain a similar spectrum shape, with a new peak appearing at 385 mV above the Fermi level (Figure 2g). We assign this feature to states related to chemisorbed hydrogen located close to the Dirac point, supported by our DFT calculations for a H atom chemisorbed to a moiré R30° (Figure 2h). As highlighted in Figure 2f, we predict that a peak appears close

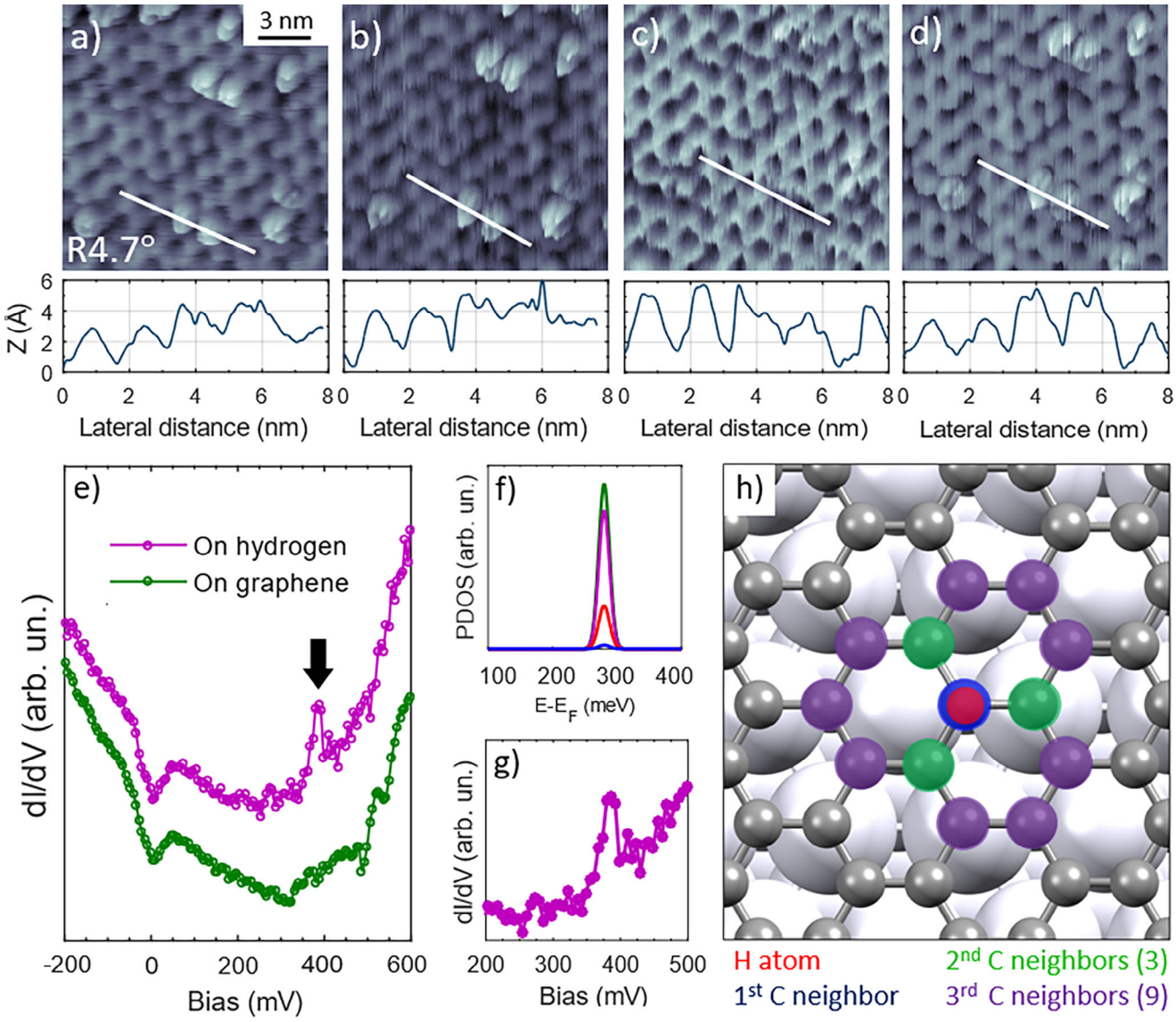

Figure 2. STM images (15 nm × 15 nm) taken at different voltages on a moiré R4.7°: a) −32 mV, b) −10 mV, c) 10 mV, d) 15 mV, e) Conductance. d*I*/d*V*, spectra acquired on a moiré R10.9° at 10 K temperature over a hydrogen cluster (purple) and on an area of bare graphene (green). A hydrogen-related peak appears at 385 mV over the Fermi level on the purple curve (black arrow). f) Projected density of states (PDOS) calculated for a moiré R30° with a chemisorbed H atom. A peak appears at 285 meV composed by the states of the 1st, 2nd and 3rd carbon neighbors (blue, green, and violet, respectively, in panel h) of the chemisorbed H atom (red). g) Zoom of the hydrogen-related peak in panel e). h) DFT calculated configuration for a H atom on a moiré R30°.

to the Dirac point, which comprises the contribution of the H atom and the neighboring C atoms. Finally, we attribute the local minimum in both STS spectra in Figure 2e, to phonon-assisted inelastic tunneling processes as reported in previous works.[44,45]

Experimentally, direct coverage comparison between different samples poses a great challenge. Hydrogen cracking requires high temperatures, and precise control of the deposition rates is only possible to some extent. The uncertainty in the deposition doses, together with tip-induced desorption (see Section S3, Supporting Information), increases the error margins when determining the density of chemisorbed clusters. However, as the amount of desorbed hydrogen during the scan depends on the measurement time, we can circumvent this difficulty analyzing images from areas in which multiple moiré domains coexist (see Figure S1a, Supporting Information for a two-domain area prior to hydrogen deposition). In **Figure 3**a,b, we show a 50 nm × 50 nm image from a graphene sample grown at 1250 K. At this temperature, we obtain a high number of smaller moiré domains covering the whole surface, with lateral sizes of some tens of nanometers and different lattice parameters. Clearly, corrugated graphene superstructures coexist with flatter areas. Out of the defective domain boundaries and at room temperature, our experimental results indicate that H clusters adsorb much more efficiently on the corrugated moirés. Figure 3c,d shows another area in which a corrugated R9° domain, with an apparent corru-

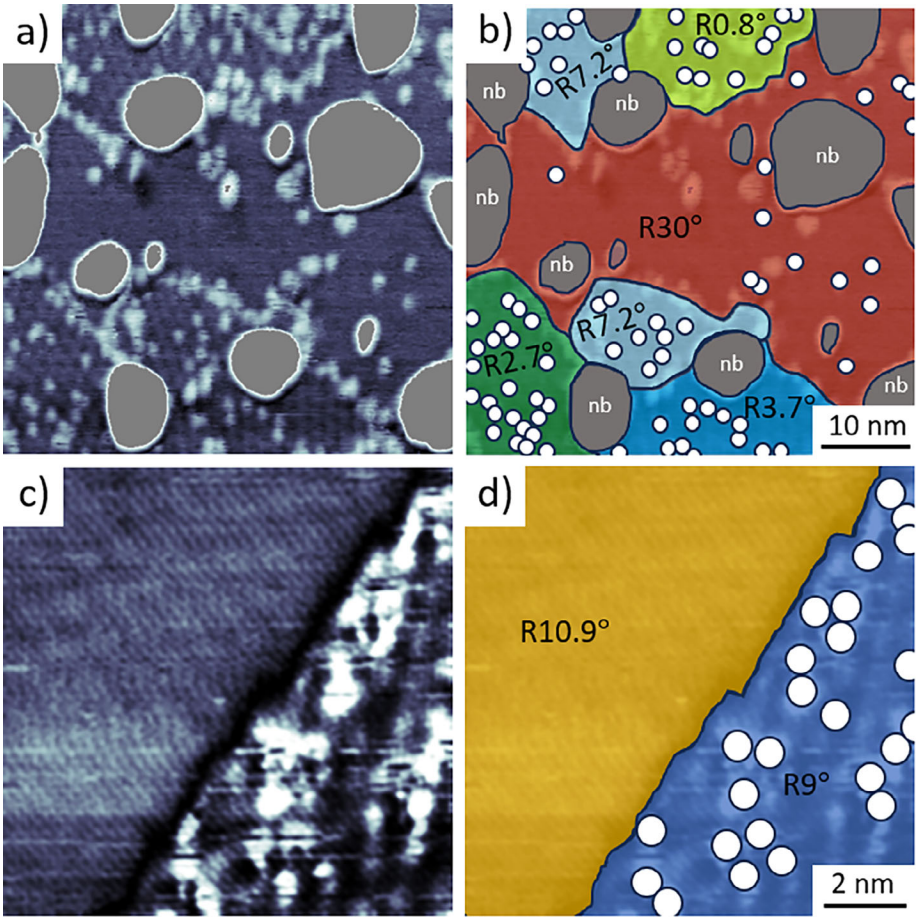

Figure 3. a) 50 nm × 50 nm STM topographic image on a region with several corrugated moiré structures coexisting with a flat moiré R30° in the center, where H clusters appear as bright protrusions. Boundaries between domains are defective areas that stabilize a considerable amount of hydrogen. Note that, out of the domain boundaries, hydrogen clearly tends to chemisorb on the corrugated patterns. b) Scheme of the different moiré domains appearing in the previous panel. White circles mark the position of H clusters adsorbed clearly outside the boundaries of the domains. Grey areas tagged as "nb" correspond to graphene nanobubbles (decoupled graphene that lifts from the surface). c) 10 nm × 10 nm STM current image of a region in which two moiré superstructures coexist after hydrogen deposition. The terrace in the left part presents a lower corrugation (moiré R10.9°) with respect to the right-hand areas (moiré R9°). The bright spots on the most corrugated area correspond to hydrogen clusters. d) Color scheme of the domains shown on the previous panel. White circles mark the position of hydrogen clusters. The boundary between the domains is an atomic step (see Figure S1c, Supporting Information for the topography image).

gation of 0.32 ± 0.02 Å, coexists with a flatter R10.9° domain, with an apparent corrugation below 0.10 Å. These two moiré patterns mark the boundary between the flat and corrugated graphene superstructures on Pt(111), which depends on the angle between the graphene and the substrate lattices and the size of the moiré supercell.[30] In this area, clusters are located exclusively on the R9° superstructure, indicating an enhanced adsorption efficiency and higher stability, in agreement with our simulations (see below).

Hydrogen chemisorption kinetics onto corrugated graphene is a multifactorial process that comprises not only the formation of a C—H bond, but also the effects of the local curvature of graphene, the interaction between neighboring H atoms and the interaction between the graphene layer and the substrate. To quantitatively understand the effect of the corrugation of the different moirés on the uptake of hydrogen and the stability of the chemisorbed atoms, we simulate the chemisorption dynamics of hydrogen with a variable-step kinetic Monte Carlo model.[37,46] In our calculations, we consider that a hot beam of H atoms at a temperature of 2300 K (corresponding to the temperature of the tungsten cracking system) arrives to a periodically modulated graphene surface at room temperature, representing the moiré superstructures of the sample. Each atom reaches the surface at a random carbon position, where it can form a C—H bond with the graphene sheet. The physisorption of H atoms or H_2 molecules is neglected as the low binding energies (in the range of 40–60 meV)[37,47–49] result in poor stability. The thermalization of the H atoms to 300 K takes some time, during which the excess of thermal energy allows for diffusion or desorption to take place. We consider that the temperature of the H atoms follows the law in Equation (1).[37]

$$T(t) = \max\left(T_{graphene}, \frac{T_{beam}}{\left(1 + B \cdot \left(t - t_{ads}\right)\right)^2}\right) \quad (1)$$

where $T_{graphene}$ and T_{beam} are the temperatures of the surface and the incoming H atoms, B is related to the thermalization speed, and t_{ads} is the time when the hydrogen atom adsorbs to the surface. Only if the hydrogen atom thermalizes before desorbing will it remain adsorbed to the surface. We consider that the reaction rates that govern the diffusion from one C atom to an adjacent one, the desorption, and the recombination from previously formed dimers follow Arrhenius law:

$$R_i\left(E_i, T\right) = A \cdot \exp\left(-\frac{E_i}{kT}\right) \quad (2)$$

In Equation (2), A is the pre-exponential factor, which we assume equal to 10^{13} Hz,[37] k is Boltzmann's constant and E_i is the energy barrier for each reaction (i = diffusion, desorption, or recombination). More details are included in Section S6.2 (Supporting Infomation) As the diffusion implies the rupture and formation of a C—H bond, the diffusion barrier essentially depends on the binding energy. We also consider the modifications in the binding energy that occur when atoms form *ortho-*, *meta-* and *para*-dimers, or other larger clusters involving more than two H atoms (in this case, for each H atom, we consider the interaction with the neighbors by pairs,[37,41] ignoring those atoms located further than the *para* positions). Doing so, we reproduce the higher binding energies expected for H atoms in large clusters.[19,25] The local curvature of the graphene sheet, d, at each carbon position is defined as the perpendicular distance of the corresponding C atom with respect to the plane defined by its three closest neighbors. According to DFT calculations from previous works,[21] the local change in the H binding energy, ΔE_B^{curv}, with respect to the flat graphene configuration, due to the local curvature follows a linear relation, and must be added to the reaction energy barriers (see also Section S6.1, Supporting Information). To account for the substrate interaction, we consider the formation of C-Pt bonds when *meta*-dimers or extended *meta*-structures are formed in areas with adequate registry with the substrate, which increases the total binding energy of the corresponding configurations. On stronger interacting substrates, such as Ir(111), this gives rise to graphane-like clusters in which one graphene sublattice is hydrogenated and the other bonds to atoms in the substrate.[19,25]

A completely accurate description of this interaction would require advanced *ab initio* calculations on all possible configurations and moiré models, which is unfeasible. However, our preliminary results on the low-interacting graphene on Pt(111) system suggest that the interaction with the substrate plays a less important role on the chemisorption of H atoms on non-defective areas than other factors such as the local curvature. This is due essentially to a decreased stability of *meta*-dimers with respect to the *para-* and *ortho*-dimers on epitaxial graphene on Pt(111) (see Sections S6.9 and S7, Supporting Information).

We simulate four deposition experiments on four different moiré models with superlattice parameters ranging from 4.9 to 19.5 Å, namely R30°, R19.1°, R9° and R2.7°. We consider a flux of 2×10^{13} atoms cm^{-2} s^{-1} and deposition times of 12 s, similar to the conditions in our experiments. The main results are summarized in **Figure 4**, where temporal snapshots of the on-surface hydrogen dynamics are displayed for t = 0, 4, 8, and 12 s. For each moiré superstructure, we incorporate an equivalent experimental image to facilitate both density and qualitative structural comparison (we note that simulations arise from stochastic processes). As in the experiments, the final configuration tends to accumulate H atoms in the convex areas of graphene, which correspond to the brightest parts in the topographic STM images (orange color in Figure 4). This is the result of three cooperative mechanisms: *i*) at the convex regions, the binding energy of the atoms is higher, and the desorption rate is lower, *ii*) the presence of previously adsorbed atoms on those areas favors the adsorption and stabilization of new H atoms in the surroundings because of the higher stability of *para-* and *ortho*-dimers, and *iii*) as the binding energy at the concave areas is lower, diffusion to those parts is slightly favorable before thermalization of the atom, moving atoms that fall in the proximities to even more unfavorable concave areas, producing desorption.

The correction in the binding energies due to the curvature of the moiré pattern is in the range of a few tenths of eV (see **Figure 5**a–h). It is useful to compare this value with the thermal energy at room temperature (300 K), kT = 0.025 eV. The rate of reaction is multiplied/divided by a factor e = 2.718 each time this value is subtracted/added to the energy barrier, according to Arrhenius law. To clarify how the correction of the binding energy due to curvature affects the adsorption and storage of hydrogen on the whole system, we simulate the time-resolved uptake/release of hydrogen on different moiré superstructures and compare them with the flat graphene. Figure 5i displays the average density of chemisorbed hydrogen atom as a function of time for 10 simulations per moiré. We find that all moirés exhibit increased hydrogen sorption capabilities with respect to flat graphene, being the figures of merit, 2.6 % and 3.2 % for the low corrugated R30° and R19.1° moiré patterns, respectively. For the highly corrugated R2.7° and R9° moirés, the adsorption of hydrogen for a flux of 10^{13} atoms cm^{-2} s^{-1} results significantly larger by an 8.0% and 9.3% increase of the amount of adsorbed H atoms after 60 s. The increased coverages for corrugated moiré superstructures reproduce the tendencies observed in STM images in multidomain areas (see Figure 3). Our results indicate that corrugation arises as a key factor to identify optimal moiré superstructures for a more efficient hydrogenation of graphene.

We have also calculated how the different moiré superstructures retain the chemisorbed hydrogen at different temperatures. To do so, as a starting point we simulate a high flux deposition saturating the surface with hydrogen for the four moiré superstructures R30°, R19.1°, R9°, and R2.7°. For comparison, we have also performed a similar simulation on a flat graphene sheet (black line in Figure 5j). A saturation coverage of 8×10^{14} atoms cm^{-2} (21% of the C sites or 1.6 wt.% of chemisorbed H) is reached in all systems after 12 s under a flux of 10^{15} atoms cm^{-2} s^{-1} (50 times higher than in that used in Figure 4). The abstraction of previously adsorbed H atoms by new incoming H atoms limits this maximum coverage. We utilize the resulting saturated configurations in desorption simulations with the kinetic chemisorption Monte Carlo model, in which we set the temperature of the graphene sheet at 300, 350, 400, and 500 K respectively. In Figure 5j we show the results for $T_{graphene}$ = 400 K after 10 simulations per moiré pattern (see Figure S8, Supporting Information for the other temperatures). At this temperature, the desorption of hydrogen takes place after few hours. The flat graphene

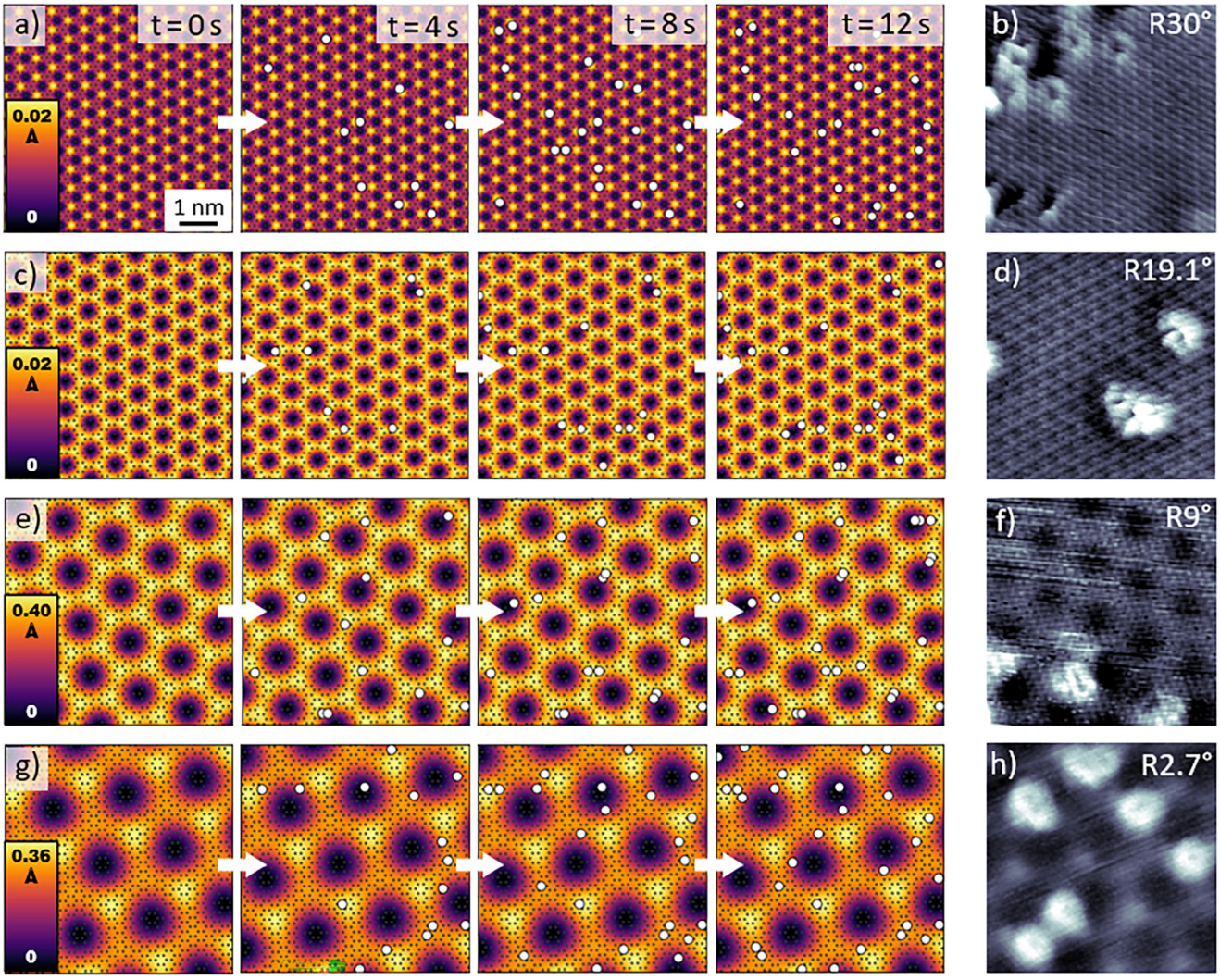

Figure 4. a,c,e,g): Snapshots from our kinetic Monte Carlo simulations of deposition of $2{\cdot}10^{13}$ H atoms·cm^{-2} s^{-1} for 12 s on the R30°, R19.1°, R9°, and R2.7° moiré patterns respectively. Experimental images are included for comparison in panels b,d,f,h) in the same order. Note that in all cases H is more stable at the more protruding parts of the moiré pattern and tends to cluster and form dimers, in agreement with our experimental images.

releases 90% of its hydrogen content after 35 min, while corrugated moiré superstructures present a slower desorption kinetics, displaying higher thermal stability and longer times of residence of the adsorbed hydrogen. Particularly, the moiré R9° system retains its hydrogen content for longer times, releasing 90% the hydrogen after 72 min at 400 K. At 350 K, similar results are found, but time scales are much longer (in the range of days, see Figure S8b, Supporting Information) in agreement with the stability of the H clusters observed in our room temperature STM experiments. At 300 K, the corrugated moiré superstructures suffer fewer thermal losses, retaining between 4 and 5 % more of their total coverage than non-corrugated superstructures after 10 days (see Figure S8a, Supporting Information).

3. Conclusion

In summary, we have conducted an extensive characterization of the chemisorption of atomic hydrogen on ten different moiré superstructures of monolayer graphene on Pt(111) by scanning tunneling microscopy and first-principles density functional theory-based calculations. Chemisorbed hydrogen forms clusters that we identify as non-magnetic dimers (*ortho-* or *para-* dimers) and accumulates in convex areas of the corrugated moiré patterns. We reproduce our experimental results with variable-step kinetic Monte Carlo simulations of H chemisorption that include the binding energy alterations due to local curvature and the clustering of H atoms, and use them to quantitatively study the effect of corrugation on the adsorption and release of chemisorbed hydrogen from graphene. Our results show that moiré corrugation has a beneficial effect on the whole system with respect to the flat graphene monolayer in both the adsorption speed and the time of residence of the chemisorbed hydrogen at different temperatures. This improvement is more pronounced for higher corrugations and lower moiré lattice parameters, as confirmed in our STM experiments.

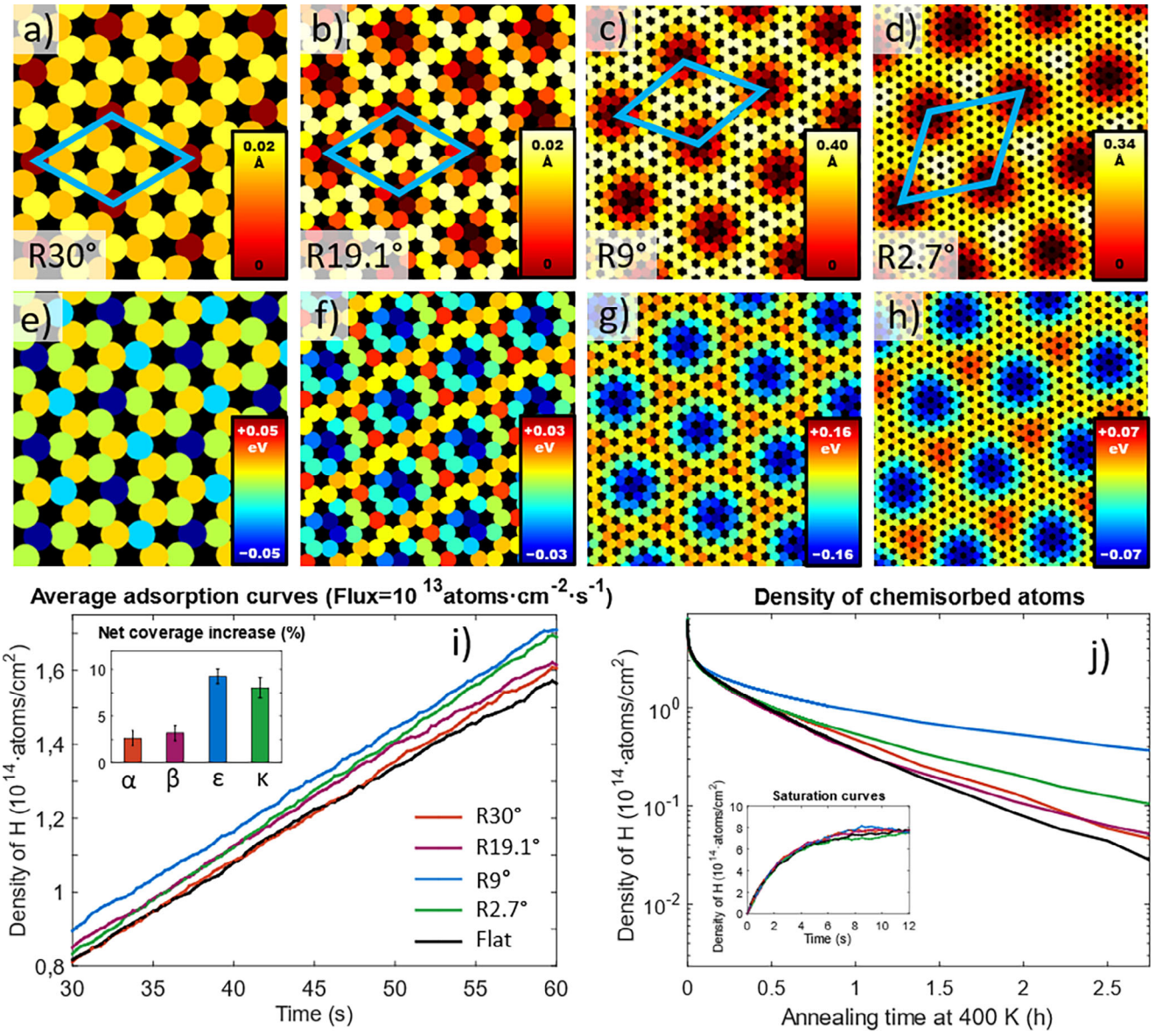

Figure 5. a–d) Topographic height for each carbon atom in the R30°, R19.1°, R9°, and R2.7° moiré superstructures respectively. Color scales indicate the height with respect to the lowest carbon atom (the closest to the Pt(111) surface). The blue rhombus in each panel corresponds to the unit cell of the pattern. e–h) indicate the binding energy modification of chemisorbed hydrogen atoms due only to the local curvature of the graphene sheet. Red colors correspond to higher binding energy and, therefore, more stable C—H bonds form on those atoms. i) Density of chemisorbed hydrogen atoms with respect to time for a flux of 10^{13} atoms cm^{-2} s^{-1}. The curves are the average of 10 different simulations. The inset shows the percentage of coverage increase with respect to the flat graphene after 60 s of deposition. j) Simulated density of chemisorbed H atoms *vs* time for saturated graphene moiré superstructures annealed at 400 K. The inset corresponds to the simulations leading to the saturation coverage for each moiré superstructure (*Flux* = 10^{15} atoms cm^{-2} s^{-1}, t = 12 s).

4. Experimental and Computational Methods

The experiments were conducted in an ultra-high vacuum chamber (UHV), P_{base} = 1×10^{-10} mbar, equipped with a home-made fullerene evaporator, a commercial thermal gas cracker (TGC-H) from SPECS for atomic hydrogen/deuterium deposition, and a room temperature scanning tunneling microscope (Omicron-STM). Unless otherwise stated, all the images were acquired in this setup at room temperature. To prepare the surface for the experiments, several sputtering-annealing cycles were performed until the surface was judged clean in the STM. For sputtering Ar^+ ions accelerated by a high voltage of 1.5 kV (typically, P_{Ar} = 3–5 × 10^{-6} mbar, I = 9–10 μA, t = 10 min) were used. It was followed by a flash-annealing at 1150 K under $P = 2 \times 10^{-7}$ mbar of oxygen to remove the carbonaceous species from previous experiments. The substrate temperature was controlled with a two-color pyrometer that automatically calculates the emissivity of the sample. After pumping the oxygen and recovering a pressure below 4 × 10^{-10} mbar, typically after 5–10 min, it was continued with a second flash-annealing at 1100 K to remove the possible

oxide species formed in the previous step. This procedure reproducibly resulted in a high-quality surface, with wide flat terraces and sharps atomic steps following the main surface crystallographic directions.

Following previous works from the group,[27] graphene monolayers were grown by on-surface thermal decomposition of fullerenes deposited on the clean Pt(111) surface at 1225–1425 K from a tantalum evaporator situated inside the UHV chamber (T_{evap} = 800 K, t = 15 min). As thermal decomposition of the molecules was only possible on the catalytic Pt surface, this procedure results in high-quality full monolayers of epitaxial graphene presenting domains with different orientations (Figure S1, Supporting Information) that give rise to different periodic moiré superstructures due to the mismatch of the graphene and the Pt(111) lattices. In this system, there are 22 stable moiré superstructures, each one defined by the angle of rotation between the graphene and the substrate lattices. The corrugation of the superstructure, which was defined as the difference between the height of the lowest and the highest C atoms with respect to the surface, was characteristic of each moiré. Even though the corrugation of a particular moiré cannot be adjusted in this system, there is a certain degree of control on the type of moiré superstructures growing during graphene synthesis. On one hand, fullerene decomposition at high surface temperatures (1325–1425 K) resulted in large noncorrugated moiré domains with smaller lattice parameters. On the other hand, deposition at lower temperatures (1225–1325 K) resulted in small moiré domains with higher lattice parameters and higher corrugations.

The hydrogen cracker consists of a tungsten capillary heated at 2300 K by electron bombardment at one of its ends and a shutter to block the beam of hot hydrogen atoms. A leak valve was used to introduce 1×10^{-8} mbar of diatomic deuterium or hydrogen gas before turning on the cracker. Once the cracking temperature was reached, the molecules dissociate thanks to the thermal energy with an efficiency close to 100 %. After that, the shutter was opened and oriented the graphene surface (T = 300 K) toward the resulting beam of hot atoms. Typically, hydrogen was deposited for 12–24 s. It was estimated that the flux of H atoms is in the range of 10^{13} atoms cm^{-2} s^{-1}, during a deposition time of 12 s for all images. This corresponds to densities of 0.03–0.15 clusters of hydrogen/nm^{-2} in the experimental images, depending on the moiré superstructure.

STM experiments at helium temperature were conducted in a different chamber equipped with a cold-finger STM (Sigma) and its own hydrogen cracker. Pristine graphene was prepared on Pt(111) samples in the previous chamber and transferred by means of a vacuum suitcase ($P_{base} = 1 \times 10^{-8}$ mbar). The inherent inertness of the graphene monolayer covering all the Pt(111) surface protected the sample form contamination during the transference. A similar amount of atomic hydrogen was deposited in the chamber, and introduced the sample in the STM stage to cool down. Scanning Tunneling Spectroscopy (STS) experiments were conducted by introducing a sinusoidal modulation to the DC bias with an amplitude of 20 mV and a frequency of 933 Hz and differentiating the tunnel current with a lock-in to obtain the conductance. The images with the WSxM software was processed and filtered.[50]

First-principles computational analysis of the $(\sqrt{3} \times \sqrt{3})$R30° H/Gr/Pt(111) α moiré superstructure was carried out by using Density Functional Theory (DFT) as implemented in the QUANTUM ESPRESSO plane-wave simulation package for determining the ground-state structure and electronic properties of the system,[51] as well as for the simulation of Tersoff-Hamann STM images.[52] See further details about the computational details and theoretical approach in Section S4 (Supporting Information).

A variable step-size kinetic Monte Carlo model, based on the work of H. M. Cuppen and L. Hornekær,[37] was used to simulate the adsorption and desorption dynamics of hydrogen on a graphene sheet. To simulate the moiré patterns, a periodical sinusoidal corrugation was introduced, whose amplitude was chosen to match previously reported moiré corrugations and lattice parameters (see Table S1, Supporting Information) and our experimental observations. In our model, a beam of H atoms arrives to the surface with a thermal energy corresponding to the cracking temperature (2300 K). The atoms chemisorb to random carbon positions from the graphene layer and were able to desorb, diffuse, and recombine thanks to the excess of thermal energy. It was assumed that the effective temperature of the chemisorbed H atoms follows Equation (1).[37] The model also includes the abstraction of a previously adsorbed H atom by an incoming atom that reaches the same position, but not other Eley-Rideal processes. The variations of the H binding energy due to the formation of *ortho*-, *meta*-, and *para*-dimers are included in the model, as well as the formation of larger clusters, for which we add the interaction with the neighboring H atoms by pairs.[37,41] The interactions with the substrate are considered indirectly as the responsible of the patterning of the graphene, which allows for the use of the model to simulate depositions on epitaxial graphene grown on other surface, such as Ir(111) (see Section S6.8, Supporting Information). During the adsorption simulations, the graphene temperature is set at 300 K, whereas for desorption simulations at high temperatures, the temperature of a previously hydrogenated substrate is selected as desired. Further details of the Monte Carlo simulations can be found in Section S6 (Supporting Information).

Supporting Information

Supporting Information is available from the Wiley Online Library or from the author.

Acknowledgements

The authors acknowledge financial support from the Spanish MICIN (grants PID2021-12509OA-I00, PID2023-149077OB-C31, TED2021-129416A-I00, TED2021-129999B-C31, RYC2024-049194-I, EUR2021-122006, and CNS2022-135658 funded by MCIN/AEI/10.13039/501100011033 and by "ERDF A way of making Europe", by "ERDF/EU" and the "European Union NextGenerationEU/PRTR") and TEC-2024/TEC-459 project funded by the "Comunidad de Madrid" and co-financed by European Structural Funds. The authors acknowledge the Severo Ochoa Centres of Excellence program through Grant CEX2024-001445-S. BC acknowledges support from the Spanish CM "Talento Program César Nombela" (project No. 2023-T1/TEC-28968). DA also acknowledges funding from the Spanish MICIN through an FPU-2019 predoctoral grant (FPU19/04556).

Conflict of Interest

The authors declare no conflict of interest.

Data Availability Statement

The data that support the findings of this study are available from the corresponding author upon reasonable request.

Keywords

hydrogen, moiré physics, graphene, scanning tunneling microscopy

Received: June 18, 2025
Revised: July 16, 2025
Published online: July 28, 2025

[1] J. Tu, M. Yan, *Small* **2024**, 2408116.
[2] I. Palacio, M. Moreno, A. Náñez, A. Purwidyantri, T. Domingues, P. D. Cabral, J. Borme, M. Marciello, J. I. Mendieta-Moreno, B. Torres-Vázquez, J. I. Martínez, M. F. López, M. García-Hernández, L. Vázquez, P. Jelínek, P. Alpuin, C. Briones, J. Á. Martín-Gago, *Biosens. Bioelectr.* **2023**, *222*, 115006
[3] Y. Gao, Z. Li, P. Wang, W.-G. Cui, X. Wang, Y. Yang, F. Gao, M. Zhang, J. Gan, C. Li, Y. Liu, X. Wang, F. Qi, J. Zhang, X. Han, W. Du, J. Chen, Z. Xia, H. Pan, *Nat. Commun.* **2024**, *15*, 928
[4] S. Banerjee, A. M. Rappe, *J. Am. Chem. Soc.* **2022**, *144*, 7181.
[5] Q. Wan, H. Guo, S. Lin, *ACS Catal.* **2022**, *12*, 14601.
[6] J.-W. Chen, S.-H. Hsieh, S.-S. Wong, Y.-C. Chiu, H.-W. Shiu, C.-H. Wang, Y.-W. Yang, T.-J. Hsu, D. Convertino, C. Coletti, S. Heun, C.-H. Chen, C.-L. Wu, *ACS Energy Lett.* **2022**, *7*, 2297.
[7] Q. He, L. Zeng, L. Han, M. M. Sartin, J. Peng, J.-F. Li, A. Oleinick, I. Svir, C. Amatore, Z.-Q. Tian, D. Zhan, *J. Am. Chem. Soc.* **2021**, *143*, 18419.
[8] A. J. Shih, N. Arulmozhi, M. T. M. Koper, *ACS Catal.* **2021**, *11*, 10892.
[9] R. A. Bueno, J. I. Martínez, R. F. Luccas, N. Ruiz del Árbol, C. Munuera, I. Palacio, F. J. Palomares, K. Lauwaet, S. Thakur, J. M. Baranowski, W. Strupinski, M. F. López, F. Mompean, M. García-Hernández, J. A. Martín-Gago, *Nat. Commun.* **2017**, *8*, 1.
[10] L. Xie, L. Wang, W. Zhao, S. Liu, E. Huang, Q. Zhao, *Nat. Commun.* **2021**, *12*, 1.
[11] Z. Jiang, W. Zhou, A. Hong, M. Guo, X. Luo, C. Yuan, *ACS Energy Lett.* **2019**, *4*, 2830.
[12] I. Brihuega, F. Yndurain, *J. Phys. Chem. B* **2018**, *122*, 595.
[13] J. H. Jørgensen, A. Čabo, R. Balog, L. Kyhl, M. N. Groves, A. M. Cassidy, A. Bruix, M. Bianchi, M. Dendzik, M. A. Arman, L. Lammich, J. I. Pascual, J. Knudsen, B. Hammer, P. Hofmann, L. Hornekaer, *ACS Nano* **2016**, *10*, 10798.
[14] Y. Yu, K. Zhang, H. Parks, M. Babar, S. Carr, I. M. Craig, M. Van Winkle, A. Lyssenko, T. Taniguchi, K. Watanabe, V. Viswanathan, D. Kwabena Bediako, *Nat. Chem.* **2022**, *14*, 267.
[15] T. Kosmala, A. Baby, M. Lunardon, D. Perilli, H. Liu, C. Durante, C. Di Valentin, S. Agnoli, G. Granozzi, *Nat. Catal.* **2021**, *4*, 850.
[16] J. J. Navarro, F. Calleja, R. Miranda, E. M. Pérez, A. L. Vázquez De Parga, *Chem. Commun.* **2017**, *53*, 10418.
[17] R. Balog, B. Jørgensen, L. Nilsson, M. Andersen, E. Rienks, M. Bianchi, M. Fanetti, E. Lægsgaard, A. Baraldi, S. Lizzit, Z. Sljivancanin, F. Besenbacher, B. Hammer, T. G. Pedersen, P. Hofmann, L. Hornekær, *Nat. Mater.* **2010**, *9*, 315.
[18] Y. Song, K. Qian, L. Tao, Z. Wang, H. Guo, H. Chen, S. Zhang, Y.-Y. Zhang, X. Lin, S. T. Pantelides, S. Du, H.-J. Gao, *Small* **2022**, *18*, 2102687.
[19] M. Andersen, L. Hornekær, B. Hammer, *Phys. Rev. B* **2012**, *86*, 1.
[20] R. Balog, B. Jørgensen, J. Wells, E. Lægsgaard, P. Hofmann, F. Besenbacher, L. Hornekær, *J. Am. Chem. Soc.* **2009**, *131*, 8744.
[21] V. Tozzini, V. Pellegrini, *J. Phys. Chem. C* **2011**, *115*, 25523.
[22] A. Nikitin, X. Li, Z. Zhang, H. Ogasawara, H. Dai, A. Nilsson, *Nano Lett.* **2008**, *8*, 162.
[23] S. Goler, C. Coletti, V. Tozzini, V. Piazza, T. Mashoff, F. Beltram, V. Pellegrini, S. Heun, *J. Phys. Chem. C* **2013**, *117*, 11506.
[24] P. Ruffieux, O. Gröning, M. Bielmann, P. Gröning, *Appl. Phys. A* **2004**, *78*, 975.
[25] R. Balog, M. Andersen, B. Jørgensen, Z. Sljivancanin, B. Hammer, A. Baraldi, R. Larciprete, P. Hofmann, L. Hornekær, S. Lizzit, *ACS Nano* **2013**, *7*, 3823.
[26] P. Merino, M. Švec, J. I. Martínez, P. Mutombo, C. Gonzalez, J. A. Martín-Gago, P. L. de Andres, P. Jelinek, *Langmuir* **2014**, *31*, 233.
[27] P. Merino, M. Švec, A. L. Pinardi, G. Otero, J. A. Martín-Gago, *ACS Nano* **2011**, *5*, 5627.
[28] M. Gao, Y. Pan, L. Huang, H. Hu, L. Z. Zhang, H. M. Guo, S. X. Du, H.-J. Gao, *Appl. Phys. Lett.* **2011**, *98*, 033101.
[29] J. I. Martínez, P. Merino, A. L. Pinardi, G. Otero-Irurueta, M. F. López, J. Méndez, J. A. Martín-Gago, *Sci. Rep.* **2016**, *6*, 2.
[30] L. Zhang, F. Ding, *ACS Appl. Mater. Interfaces* **2021**, *13*, 56674.
[31] L. Hornekær, W. Xu, R. Otero, E. Lægsgaard, F. Besenbacher, *Chem. Phys. Lett.* **2007**, *446*, 237.
[32] E. Cortés-del Río, P. Mallet, H. González-Herrero, J. L. Lado, J. Fernández-Rossier, J. M. Gómez-Rodríguez, J.-Y. Veuillen, I. Brihuega, *Adv. Mater.* **2020**, *32*, 1.
[33] R. Balog, A. Cassidy, J. Jørgensen, L. Kyhl, Mie Andersen, A. G. Čabo, F. Ravani, L. Bignardi, P. Lacovig, Silvano Lizzit, *J. Phys. Condens. Matter* **2019**, *31*, 085001.
[34] Y. Ferro, D. Teillet-Billy, N. Rougeau, V. Sidis, S. Morisset, A. Allouche, *Phys. Rev. B.* **2008**, *78*, 085417.
[35] H. González-Herrero, J. M. Gómez-Rodríguez, P. Mallet, M. Moaied, J. J. Palacios, C. Salgado, M. M. Ugeda, J.-Y. Veuillen, F. Yndurain, I. Brihuega, *Science* **2016**, *352*, 437.
[36] Ž. Šljivančanin, M. Andersen, L. Hornekær, B. Hammer, *Phys. Rev. B.* **2011**, *83*, 205426.
[37] H. M. Cuppen, L. Hornekær, *J. Chem. Phys.* **2008**, *128*, 174707.
[38] Ž. Šljivančanin, E. Rauls, L. Hornekær, W. Xu, F. Besenbacher, B. Hammer, *J. Chem. Phys.* **2009**, *131*, 084706.
[39] L. Nilsson, M. Andersen, R. Balog, E. Lægsgaard, P. Hofmann, F. Besenbacher, B. Hammer, I. Stensgaard, L. Hornekær, *ACS Nano* **2012**, *6*, 10258.
[40] D. Lizzit, et al., *ACS Nano* **2019**, *13*, 1828.
[41] M. Moaied, J. A. Moreno, M. J. Caturla, F. Ynduráin, J. J. Palacios, *Phys. Rev. B* **2015**, *91*, 155419.
[42] Y. Tong, Y. Yang, *J. Phys. Chem. C* **2024**, *128*, 840.
[43] P. Sutter, J. T. Sadowski, E. Sutter, *Phys. Rev. B* **2009**, *80*, 245411.
[44] N. Levy, S. A. Burke, K. L. Meaker, M. Panlasigui, A. Zettl, F. Guinea, A. H. Castro Neto, M. F. Crommie, *Science* **2010**, *329*, 544.
[45] Y. Zhang, V. W. Brar, F. Wang, C. Girit, Y. Yayon, M. Panlasigui, A. Zettl, M. F., *Nat. Phys.* **2008**, *4*, 627.
[46] A. P. J Jansen, *Comput. Phys. Commun.* **1995**, *86*, 1.
[47] V. Jain, B. K. subramanian, *J. Mater. Sci.* **2020**, *55*, 1865.
[48] H. González-Herrero, E. Cortés-del Río, P. Mallet, J.-Y. Veuillen, J. J. Palacios, J. M. Gómez-Rodríguez, I. Brihuega, F. Ynduráin, *2D Mater.* **2019**, *6*, 021004.
[49] M. Bonfanti, S. Achilli, R. Martinazzo, *J. Phys. Condens. Matter* **2018**, *30*, 283002.
[50] I. Horcas, R. Fernández, J. M. Gómez-Rodríguez, J. Colchero, J. Gómez-Herrero, A. M. Baro, *Rev. Sci.* **2007**, *78*, 013705.
[51] P. Giannozzi, S. Baroni, N. Bonini, M. Calandra, R. Car, C. Cavazzoni, D. Ceresoli, G. L. Chiarotti, M. Cococcioni, I. Dabo, *J. Phys. Condens. Matter* **2009**, *21*, 395502.
[52] J. Tersoff, D. R. Hamann, *Phys. Rev. B* **1985**, *31*, 805.